Spatially resolved mapping of disorder type and distribution in random systems using artificial neural network recognition

A. Kumar,[1] O. Ovchinnikov,[2] S. Guo,[1] F. Griggio,[3] S. Jesse,[1] S. Trolier-McKinstry,[3] and S.V. Kalinin[1,3,*]

[1]*The Center for Nanophase Materials Science, Oak Ridge National Laboratory, Oak Ridge, Tennessee 37831, USA*

[2]*Department of Physics and Astronomy, University of Tennessee, Knoxville, Tennessee, USA*

[3]*Department of Materials Science and Engineering and Materials Research Institute, Pennsylvania State University, University Park, Pennsylvania 16802, USA*

(Received 21 February 2011; published 6 July 2011)

The spatial variability of the polarization dynamics in thin film ferroelectric capacitors was probed by recognition analysis of spatially resolved spectroscopic data. Switching spectroscopy piezoresponse force microscopy (SSPFM) was used to measure local hysteresis loops and map them on a two dimensional (2D) random-bond, random-field Ising model. A neural-network based recognition approach was utilized to analyze the hysteresis loops and their spatial variability. Strong variability is observed in the polarization dynamics around macroscopic cracks because of the modified local-elastic and electric-boundary conditions, with the most pronounced effect on the length scale of ∼100 nm away from the crack. The recognition approach developed here is universal and can potentially be applied for arbitrary macroscopic and spatially resolved data, including temperature- and field-dependent hysteresis, I-V curve mapping, electron microscopy electron energy loss spectroscopy (EELS) imaging, and many others.

DOI: 10.1103/PhysRevB.84.024203 PACS number(s): 77.80.Fm, 61.43.−j, 07.79.Lh

I. INTRODUCTION

Disorder attributable to point, extended, and volume defects is ubiquitous in condensed-matter systems ranging from strongly correlated magnetoresistive oxides,[1] superconductors,[2] metal-insulator systems,[3] spin and cluster glasses,[4] and ferroelectric relaxors[5] to polycrystalline films and ceramics. Despite the broad range of underpinning structural and physical mechanisms, these systems often exhibit similar types of time and field dynamics, allowing for classification in terms of small number of universality classes. The universality classes can be related to statistical physics models[6] and, in many cases, can be established based on macroscopic measurements such as the temperature or field dependence of characteristic properties in the vicinity of the phase-transition points, as well as the phenomenological information about the structure and underpinning interactions.[7]

However, in many materials, the structural disorder develops across multiple length scales. As a prototypical example, in polycrystalline ceramics or films, inhomogeneities of vacancy or cation distributions lead to the atomic-level disorder, with the domain textures and extended defects forming the next structural level, and grains boundaries separating crystallites with length scales extending to micron range. Similarly, many ferroic materials form hierarchical domain structures or textures, with this tendency being especially pronounced in the vicinity of ferroelectric-antiferroelectric or morphotropic-phase boundaries. Macroscopic property measurements will necessarily sample the collective effects arising from all these length scales, and decoupling of these effects (e.g., using impedance type measurements) is subject to multiple uncertainties. The situation is further complicated by the fact that in many cases the material response is hysteretic in nature, precluding description by linear models. A number of groups are exploring identification of disorder based on the systematic analysis of macroscopic-hysteresis loops and minor-hysteresis loop families;[8–10] however, relating this behavior to individual microstructural elements remains a challenge.

Recently the study of materials on the nanoscale has allowed probing of responses dominated by finite size effects,[11,12] thus providing insight into local behavior. As an alternative to fabricating isolated nanoscale structures, the emergence of high-resolution imaging techniques enables spatially resolved observations of the geometry of static and moving interfaces in disordered systems.[13–16] This approach requires careful analysis of finite image size, random noise, and resolution effects on data analysis.[17] The disorder class can be identified based on fractal dimensionality of the front geometry or other statistical descriptors of the system, but the variations in type and strength of disorder between adjacent locations remain inaccessible.

Here we explore an approach for the identification and spatially resolved mapping of strength and type of disorder in complex physical systems based on the combination of spectroscopic-hysteresis loop imaging and neural-network recognition fitting onto a selected statistical physics model.[18] As a model system, we have chosen columnar ferroelectric capacitors,[19] previously extensively studied in the piezoresponse force microscopy imaging.[20–24] The local hysteretic responses are mapped onto a two-dimensional (2D) random-bond, random-field Ising model at zero temperature, and the spatial variability of corresponding disorder parameters is mapped down to nanometer scales.

II. MAPPING LOCAL-POLARIZATION DYNAMICS BY BAND EXCITATION (BE) SWITCHING SPECTROSCOPY PIEZORESPONSE FORCE MICROSCOPY (SSPFM)

The ferroelectric capacitors used in this study are prepared from a sol-gel deposited $(0.3)Pb(Ni_{0.33}Nb_{0.67})O_3$–$(0.7)Pb(Zr_{0.45}Ti_{0.55})O_3$ thin film (corresponding to the

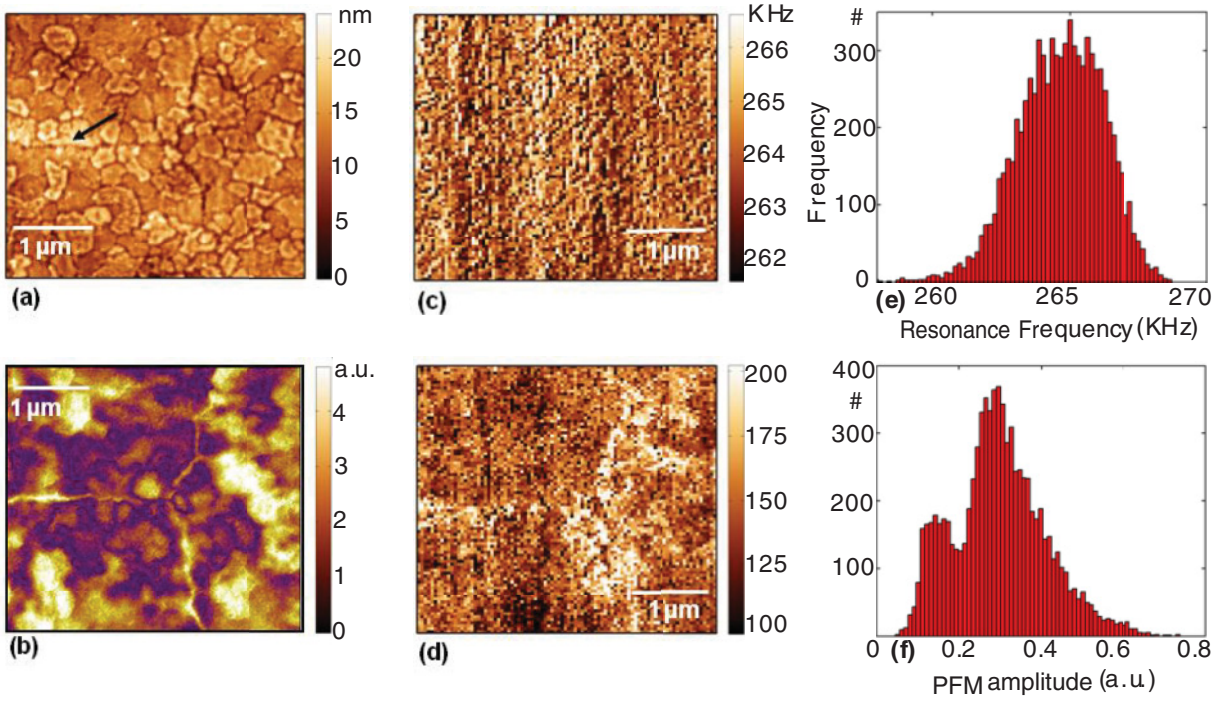

FIG. 1. (Color online) (a) Surface topography (arrow indicates the propagating crack), (b) PFM image collected at 250 kHz using a probing amplitude of 1V, (c) resonance frequency, and (d) Q-factor images of the polycrystalline capacitor surface. Histograms of (e) resonance frequency and (f) PFM amplitude obtained across the surface.

morphotropic phase boundary composition) with top and bottom platinum electrodes.[25,26] The film thickness was 630 nm, which was large enough to exceed the critical thickness for cracking attributable to the thermal expansion coefficient mismatch between the material and the Si substrate. The average coercive voltage for this film was 1.9 V, corresponding to a coercive field of 29 kV/cm. Field emission scanning electron microscopy images revealed a dense and large-grained microstructure with an average grain size of 200 ± 80 nm. X-ray diffraction (XRD) analysis showed pure perovskite phase with 80% {001} texture as determined using the Lotgering formula.[27] Before performing switching spectroscopy measurements, the film was poled by applying 10 V to the top electrode for 15 minutes.

In many proper ferroelectric films the domains interact across grain boundaries because of local electric and elastic fields[28] and also experience the random fields because of defects and top and bottom interfaces. Spatially resolved switching studies of similar materials without top electrodes have demonstrated that the polarization switching typically occurs uniformly within the grains.[29] The typical switching fields are of the order of several volts, thus minimizing the role of spontaneous thermally activated polarization reversal. These considerations suggest that the salient features of system behavior can be approximated by random-field, random-bond 2D Ising model, with the spontaneous polarization in regions of correlated switching inside individual columnar grains playing the role of Ising spins; random electric fields because of charged defects and interfaces playing the role of on-site random fields; and grain-grain coupling, fluctuations in Zr/Ti ratio, and rhombohedral/tetragonal phase stability playing the role of random-bond component. We further note that while in the bulk materials the applicability of the Ising model is necessarily limited by the long range of the depolarization, strain, and electrostatic fields, in thin films these interactions are screened on a length scale on the order of the film thickness.

To obtain a system with defects at several length scales, a region on the capacitor surface with a well-defined macroscopic crack was chosen, as shown in Fig. 1. The topographic image shows an average grain size of 246 ± 110 nm and noticeable topographic contrast corresponding to the three cracks forming a junction point at the center of the imaged region. We note that interpretation of the local Piezoresponse Force Microscopy (PFM) data on the capacitor-type structures should include both local effects attributable to response of material directly below the tip, as well as surface acoustic waves and any bending bimorph modes of the device.[29]

To explore the spatially resolved switching behavior in the capacitor structure, BE PFM[30–34] and BE SSPFM were utilized. A modest (0.5–2 V_{pp}) BE bias is applied between the two electrodes, resulting in an electromechanical response of the surface that is detected by an scanning probe microscopy (SPM) tip. The PFM and SSPFM were implemented on a commercial Asylum Cypher system with additional in-house electronics for BE and SSPFM measurements based on an NI PXI platform (National Instruments). For measurements made on electroded areas, the bottom electrode was grounded, while the voltage was applied simultaneously to the tip and the top electrode. The electrodes were connected through wirebonds to an external bias source. Vertical PFM and SSPFM measurements were performed near the contact resonance of the tip-sample configuration in order to obtain

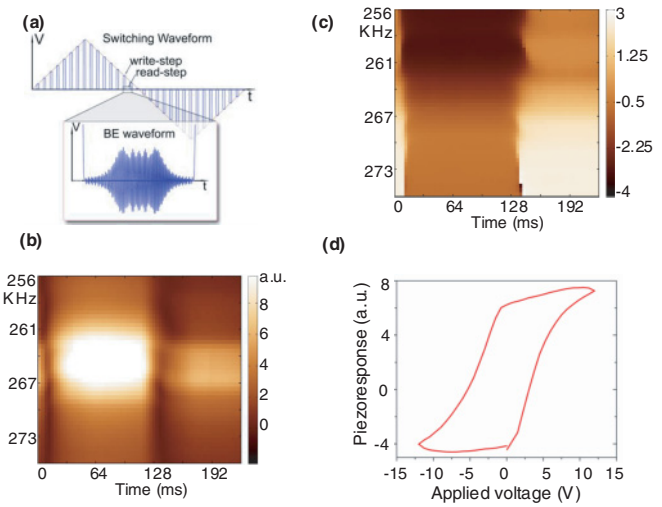

FIG. 2. (Color online) Data acquisition and processing in band excitation switching spectroscopy PFM. (a) At a single spatial location, the switching signal is formed by the triangular waveform modulated by rectangular pulses. The on-state pulse induces switching, while the electromechanical response is detected in the off-state in a broad frequency range centered at the tip-surface resonance using a band-excitation waveform. At each pixel, the measured amplitude response represents a 2D (b) amplitude and (c) cantilever response phase versus frequency and time spectrogram. The evolution of amplitude and phase with applied DC waveform is clearly seen. (d) The signal in the 2D spectrogram is (i) integrated over the frequency axis or (ii) fitted by a simple harmonic oscillator (SHO) model to yield the single-point hysteresis loops.

high signal-to-noise ratio through resonance-enhancement. Pt-coated conductive tips (Olympus AC240TM) were used for the SSPFM studies. To implement BE SSPFM, the tip was first brought to contact the sample surface. Once the tip established contact, a triangular waveform composed of a sequence of pulses with increasing DC bias (12 V maximum) at a constant time interval was applied, as shown in Fig. 2(a). The bias pulse was used to switch the sample. A chirp excitation with a predefined frequency band and amplitude (1 V) was applied to the tip during interval between two pulses as shown in Fig. 2(a), and the mechanical tip response was simultaneously registered at this interval. Details of hysteresis-loop extraction from the obtained data are provided below. A LABVIEW-MATLAB code developed in-house and synchronized with the controller was used for generating the probing signal and for data acquisition and analysis.

The excellent vertical resolution of scanning probe microscopy allows displacements as small as ∼3–10 pm to be detected locally at an integration time for the data acquisition card of ∼1 ms. In capacitor experiments the effective lateral resolution (probed-lateral size) is determined by the surface strain distribution induced by a uniform electric field and can be estimated as ∼(0.2–0.5) H + (0.5–1) L, where H is the ferroelectric thickness and L is the top electrode thickness.[35] Here we estimate spatial resolution as ∼150–400 nm, in the vicinity of the observed grain size for this film. Note that in the case where there is either weak mechanical contact between the grains or strong variations in the electromechanical activity in the surface layers of the film, features visible at higher resolution might be detected. Finally the macroscopic-bending modes of the substrate localized on the length scale of the Si-substrate thickness can give rise to offsets in measured PFM images and spectroscopic data.[35]

To improve the signal-to-noise ratio in the PFM imaging and minimize topographic cross talk, we utilize the BE method.[36] Briefly the PFM signal is the oscillatory surface response determined as a product of driving voltage V_{ac}, electromechanical response $d_{33,\text{eff}}$, and contact/cantilever transfer function $F(\omega)$ as $PR = V_{ac} d_{33,\text{eff}} F(\omega)$. The use of resonance enhancement [$F(\omega) = 1$ for low frequencies and $F(\omega) = Q$ at the contact/cantilever resonance, where Q is of the order of 30–100 for contact resonances] is limited by the strong position dependence of contact resonance.[37–39] The use of BE [Fig. 2(a)], or equivalent methods (e.g., pulse excitation,[40,41] dual frequency measurements,[42] fast lock-in sweeps,[43] or rapid multifrequency imaging),[44] allows efficient tracking of the resonance response in PFM and, hence, high-fidelity spectroscopic measurements.[45,46] In the BE experiment the full amplitude and phase versus frequency curve is measured in a preselected frequency interval chosen to contain the tip-surface resonance peak. The data is analyzed using a simple harmonic oscillator (SHO) fit to extract the response amplitude at resonance, resonant frequency, and Q-factor.

Shown in Fig. 1(b) is the PFM-amplitude image of the capacitor surface collected at a frequency of 250 kHz. The cracks are seen as regions with slightly enhanced electromechanical activity. In addition a number of grain-like regions of enhanced and lowered electromechanical activity are now visible with feature size of around 300–500 nm. The histogram in Fig. 1(f) shows a relatively broad distribution of the PFM amplitude across the scanned surface. The corresponding resonant frequency image obtained using BE SSPFM shows primarily noise that is likely to be associated with small-scale surface roughness of the top electrode. This behavior is expected since the local resonance frequency is influenced primarily by topographic features comparable to the tip-surface contact radius, and hence its variation reflects the variability of surface topography at small length scales. The lack of systematic changes in the slow-scan axis direction, or abrupt jumps in resonance frequency between scan lines, suggest the absence of gradual tip wear or failure. We also note that the fact that resonance frequency does not show anomalies in the crack area suggests that the electrode delamination does not occur, and geometric or topographic effects do not influence the switching behavior around the crack significantly. Also the negligible resonance frequency shift suggests that the crack is quite shallow and the tip does not penetrate into the crack by more than 5 nm as compared to the electrode thickness of 40 nm. The corresponding histogram is shown in Fig. 1(e) and illustrates that the variation frequency on the surface is ∼8 kHz as compared to the resonant peak width of the order of ∼4 kHz. This consideration illustrates the need for BE imaging since the use of constant-frequency PFM in the vicinity of the resonance would result in the spurious changes of measured signal by a factor of ∼30–100 because of changes in relative difference between driving and contact-resonance frequencies.[45] Finally the Q-factor image (again averaged over the hysteresis loop) is relatively featureless with slightly enhanced Q-factor in the region of the crack. Comparison

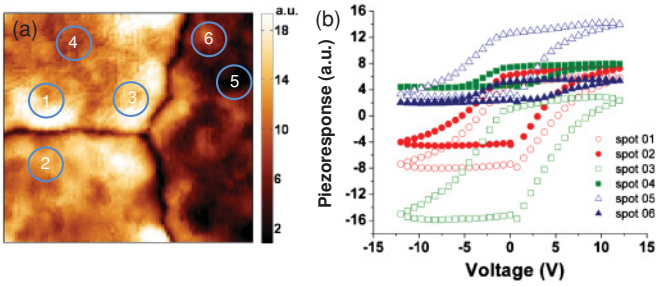

FIG. 3. (Color online) (a) Switchable polarization map and (b) hysteresis loops at selected locations across the capacitor surface from the same region as Fig. 1.

with the BE PFM amplitude image suggests that the apparent increase of the Q-factor observed near the crack is probably an artifact related to the fitting procedure (effective peak narrowing in the presence of the higher white noise floor). Correspondingly, this dissipative behavior, while of interest both for applications and fundamental energy loss processes in ferroelectrics, is deferred for future studies.

To explore polarization switching in the capacitor structure, we employ Piezoresponse Force Spectroscopy (PFS).[47–52] In PFS a probing AC signal is superimposed on the top of the DC switching signal. The evolution of electromechanical response with periodic (typically a stepped triangular wave) DC bias provides the local analog of an electromechanical hysteresis loop. Similar to imaging, we utilize the BE version of PFM spectroscopy (BEPS)[53] in order to minimize topographic cross talk and increase signal-to-noise ratio through the use of cantilever resonances. Finally in the SSPFM experiment, the hysteresis loops are acquired on a grid of points, providing spatially resolved information on the switching behavior.[54]

The waveform used for probing switching at a single location is shown in Fig. 2(a). The typical imaging conditions used here correspond to 128 frequency bins and 64 voltage points per loop. Shown in Fig. 2(b) is the typical single-point amplitude response in BE SSPFM measurements, representing the simultaneous measurement of response as a function of frequency and applied DC waveform. The single-point phase response in the measurement is shown in Fig. 2(c). These 2D spectrograms are the basic measured signal in BE SSPFM measurements and are acquired at each location on the spectral image grid. The envelope of voltage sweep versus time is a triangular wave. Here the signal is analyzed using direct integration of the area under the peak (in the frequency

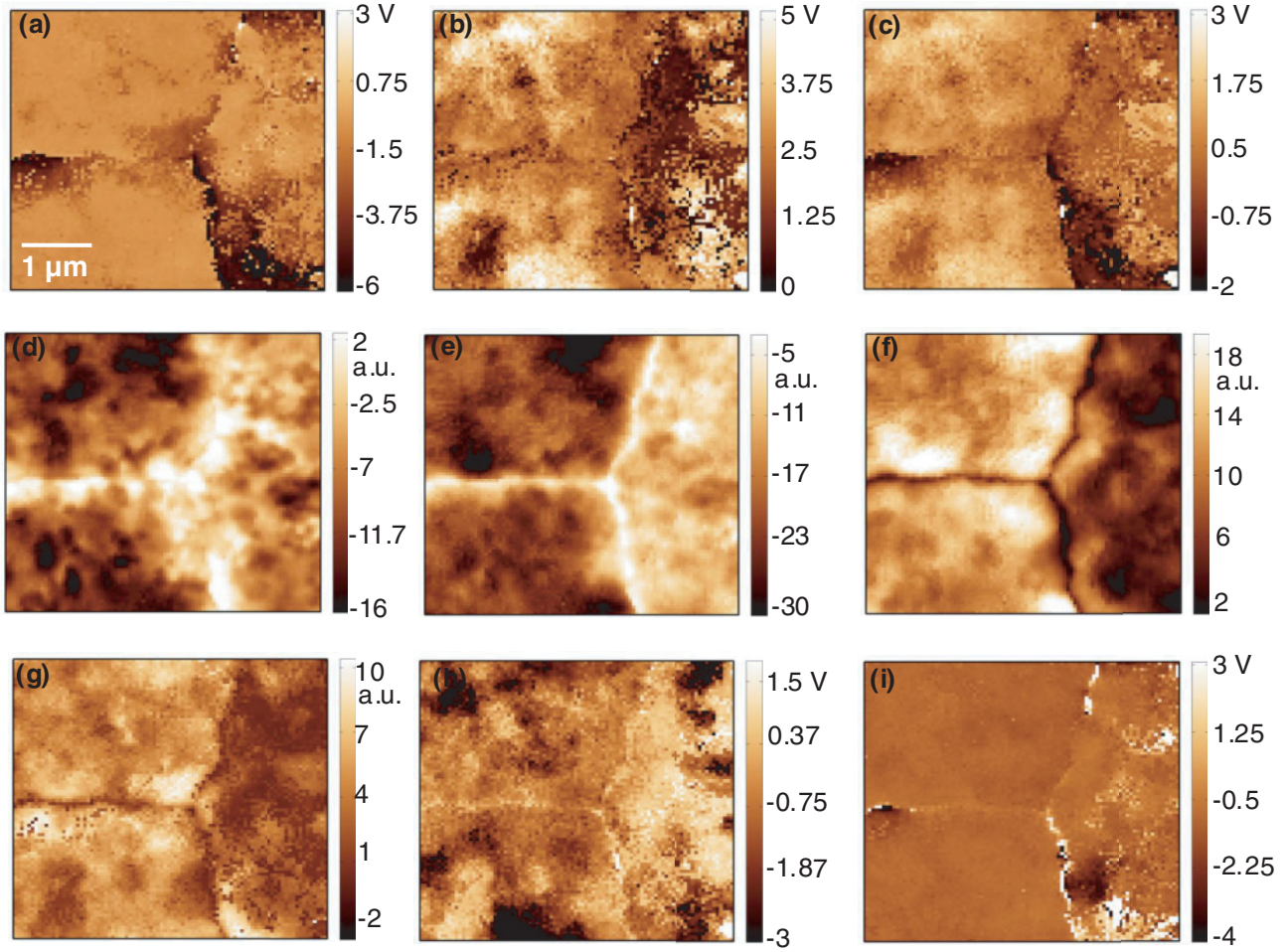

FIG. 4. (Color online) Switching parameters of the selected region on the surface. Shown are (a) positive coercive field, (b) negative coercive field, (c) imprint, (d) positive remanent response, (e) negative remanent response, (f) switching polarization, (g) work of switching, (h) positive nucleation bias, and (i) negative nucleation bias, as extracted from the experimental spatially resolved hysteresis loops array.

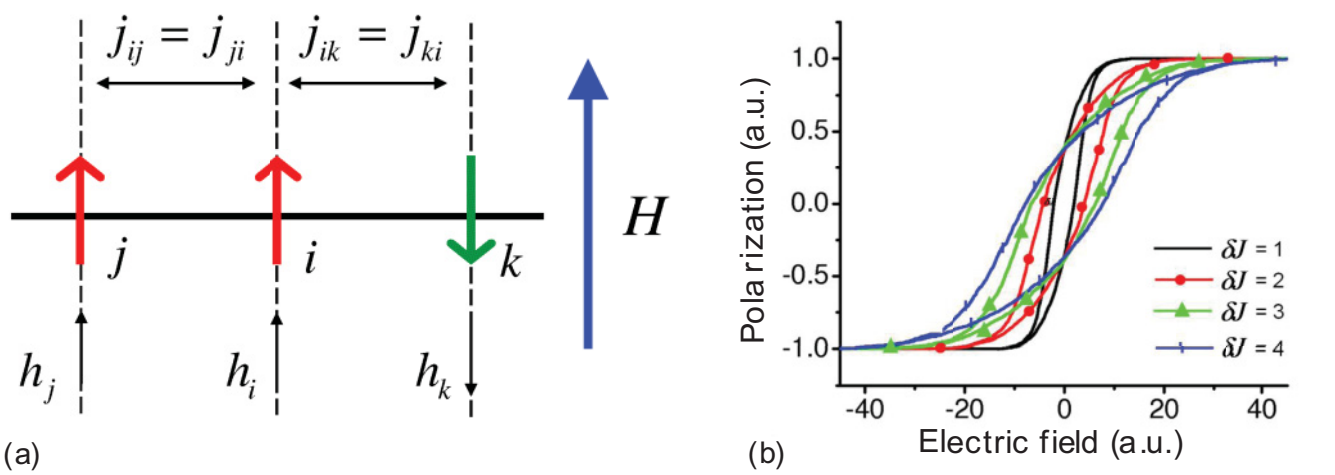

FIG. 5. (Color online) (a) 2D random-bond, random-field Ising model describing grain-grain interactions J_{ij} in the random field of defects h_i. (b) Hysteresis loops for $J = 0$, $\delta h = 0$, and $\delta J = 1, 2, 3, 4$ calculated for continuous field sweep.

direction), allowing hysteresis loops to be obtained as shown in Fig. 2(d). Alternatively the frequency-dependent data can be fitted using either a SHO or a more complex model, giving rise to the hysteresis loops for associated parameters (e.g., amplitude, phase, resonant frequency, and dissipation for SHO model).

Shown in Fig. 3(a) is the map of the switchable polarization across the surface. The hysteresis loops at several grains surrounding the cracks are shown in Fig. 3(b), showing significant changes in vertical offset and switchable polarization as well as variation in shape. This behavior is further illustrated in Fig. 4, showing a full set of SSPFM maps extracted from fitting the experimental hysteresis loops to an empirical model.[54] Strong contrast around the crack and adjoining grains is observed in the switching parameters. Both forward and reverse coercive fields are smaller in magnitude close to the crack boundary. The imprint (lateral shift) is uniform in the different grains, but the region around the crack shows shift towards negative values. Both switchable polarization and work of switching are reduced at the crack. Also note the variation of the signal between the regions separated by the crack system. The positive and negative nucleation biases on the crack are slightly enhanced with respect to the bulk of the grains. Note that the variability of switching behavior in the vicinity of the crack is expected since the strain state of the film around the crack is modified (i.e., film is clamped to the substrate far from the crack region and only partially clamped in the vicinity of the crack). Since internal stresses couple to the effective piezoelectric coefficient, domain wall mobilities, internal bias, and hence overall switchability, the modification of switching behavior is expected. It should be noted that there does appear to be a correlation between the switching polarization and distance away from the crack. Namely, there is an increase in the observed switching polarization in regions adjacent to the crack, which decreases as a function of distance from the crack.

The data in Figs. 3 and 4 illustrates the presence of significant spatial variability of the polarization switching in the capacitor and strong effect of microstructure on this behavior. However, despite the readily observed contrast, direct interpretation in terms of materials parameters is limited by lack of appropriate physical models. In the tip-electrode PFM experiment, the electric field is concentrated in the small volume of material below the tip, allowing for deterministic models.[55–61] However, in measurements of switching on top electrodes the field is almost uniform, and hence switching is initiated at the nucleation sites in the material and not necessarily directly below the probe, precluding the development of deterministic physical models. Here we analyze the data using recognition analysis that allows extraction of model parameters from the hysteresis loop by directly mapping them on relevant statistical physics model (or potentially any numerical model).

III. RECOGNITION DATA ANALYSIS

A neural-network based recognition approach was used for the analysis of the hysteresis loops.[18] In a classical approach the data analysis is performed using the known analytical form of response and use of least-square minimization (e.g., using Levenberg-Marquart search) to extract model parameters from measured data (and obtain an estimate of the applicability of the model). However for many classes of practical problems, an analytical description is absent, and the dimensionality of parameter space is sufficiently high to preclude direct search methods. The neural network approach operates in a complementary manner reminiscent of "recognition" in human brain, combining the universality of associative approach with the precision of a mathematical model.

A. Theoretical response

The system dynamics were modeled using a generalized random-bond, random-field Ising model. The Hamiltonian for this system is defined as

$$\mathrm{H}(H) = \sum_{i,j} J_{ij} S_i S_j + \sum_i (h_i + H) S_i, \qquad (1)$$

where $S_i = \pm 1$ are local dipoles, J_{ij} are nearest-neighbor interactions, h_i are random fields, and H is the external field. The nearest-neighbor interactions are assumed to have a Gaussian distribution with average J_0 and width δJ. The random-field components are assumed to have a Gaussian distribution with zero average and width δh as shown in Fig. 5(a). The simulation of Eq. (1) in the presence of external fields yields a hysteresis loop $S(H)$ as a function of model parameters, $(J_0, \delta J, \delta h)$ as shown in Fig. 5(b). The time dependence of the field is chosen similar to that used experimentally [realistic switching bias waveform as shown in Fig. 2(a), with the total polarization of the system determined in the field-off state after the application of field pulse].

For given model parameters $(J_0, \delta J, \delta h)$, the evolution of the system was studied on a 2D (10×10) field using Glauber dynamics.[6] At each time step the polarization is assumed to flip if it is antiparallel to the local field $h^i_{\rm loc} = \sum_j J_{ij} S_j - (H + h_i)$, i.e., for $h^i_{\rm loc} S_i < 0$. For $h^i_{\rm loc} S_i > 0$ the spin is stable. At each field value H the polarization values are updated randomly until for 100 iterations the average polarization $\langle S_i \rangle$ does not change. The resulting hysteresis loop $S_H = \langle S_i(H) \rangle$ defines the field dependence of average polarization averaged over 40 realizations of disorder.

B. Recognition analysis

To extract model parameters from experimental hysteresis loops, we utilize the nonparametric-deconvolution method based on a combination of principal value decomposition[62] with neural-network interpolation[63] as shown in Fig. 6.

The family of theoretical hysteresis loops $S_H(J_0, \delta J, \delta h)$ is generated using Eq. (1) in the parameter interval $J_0 \in (J_{\rm min}, J_{\rm max})$, $\delta J \in (\delta J_{\rm min}, \delta J_{\rm max})$, and $\delta h \in (\delta h_{\rm min}, \delta h_{\rm max})$, where $\delta h_{\rm min}$ is positively defined. Note that while the chosen 2D field is relatively small, the necessity to run simulations for a large number of families in the three dimensional (3D)-parameter space results in large computation times (~5–10 days on a quad-core i7 computer with 8GB of RAM).

The dimensionality of the data set containing P points in field direction is reduced using principal component analysis (PCA).[63,64] In PCA the hysteresis loops are represented as a superposition of the eigenvectors w_j,

$$S_m(H_j) = a_{mk} w_k(H_j), \tag{2}$$

where $a_{mk} = a_k(J_0, \delta J, \delta h)$ are expansion coefficients. The eigenvectors $w_k(H)$ and the corresponding eigenvalues λ_k are found from the covariance matrix $\mathbf{C} = \mathbf{S}\mathbf{S}^T$, where $\mathbf{S}$ is the matrix of all experimental data points S_{mj}. The rows of $\mathbf{S}$ correspond to parameter variation (m is the total number of hysteresis loops in a family), and columns correspond to field points. Mathematically the eigenvalues and corresponding eigenvectors are determined through singular value decomposition of the $\mathbf{S}$ matrix.[65] The number of significant values m is chosen based on the presence of correlations in the a_{mk} maps.[66] The eigenvectors $w_k(H)$ are orthonormal and are ordered such that corresponding eigenvalues are placed in descending order, $\lambda_1 > \lambda_2 > \cdots$. Consequently the first eigenvector $w_1(H)$ contains the most common information within the data set, the second contains the most common response after the subtraction of the first one, and so on. Practically, the sum in Eq. (2) can be truncated after the first several terms. This representation reduces the number and decorrelates the independent variables. In our modeling 10–15 principal components are sufficient to represent a response signal containing 8100 points.

The resulting parameter vector is used to train a feed-forward neural network with the set of $a_k(J_0, \delta J, \delta h)$ as inputs and the corresponding $J_0, \delta J, \delta h$ as target outputs. Typically for m input neurons (corresponding to the number of significant PCA components) the optimal results are obtained with (2–3)m neurons in the hidden layer using sigmoidal (*tansig*) and linear (*purelin*) transfer functions in the hidden and output layers correspondingly. Here we used a feed-forward neural network with 10 principal components, 24 hidden neurons, and 3 outputs. For optimal fitting, the overall error decreased by ~2–3 orders of magnitude compared to initial value. The increase in the number of PCA components or hidden-layer neurons

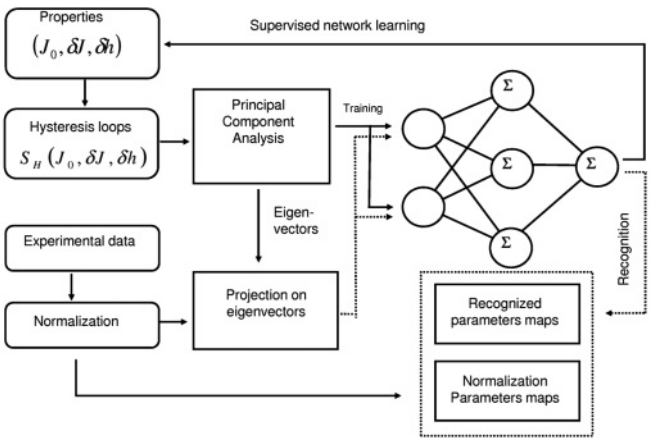

FIG. 6. Schematics of recognition analysis of experimental data utilizing principal-component-analysis based decorrelation and neural-network recognition.

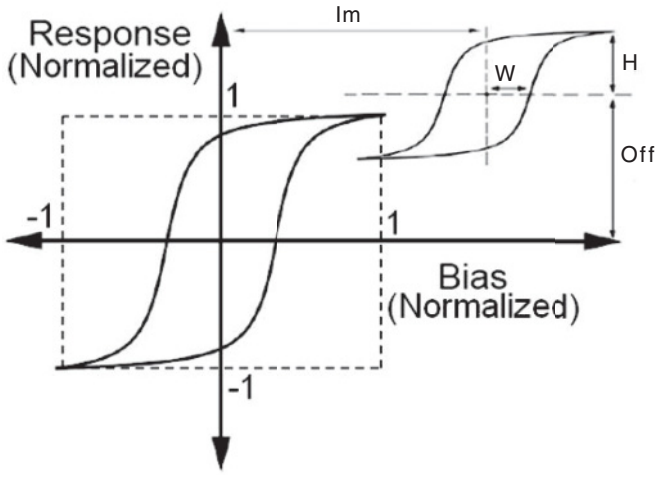

FIG. 7. Schematics of the normalization process applied to experimental data. The loops are shifted in vertical and lateral directions and normalized to unity. Thus extracted parameters are stored as imprint, Im; width, W; height, H; and vertical offset, Off.

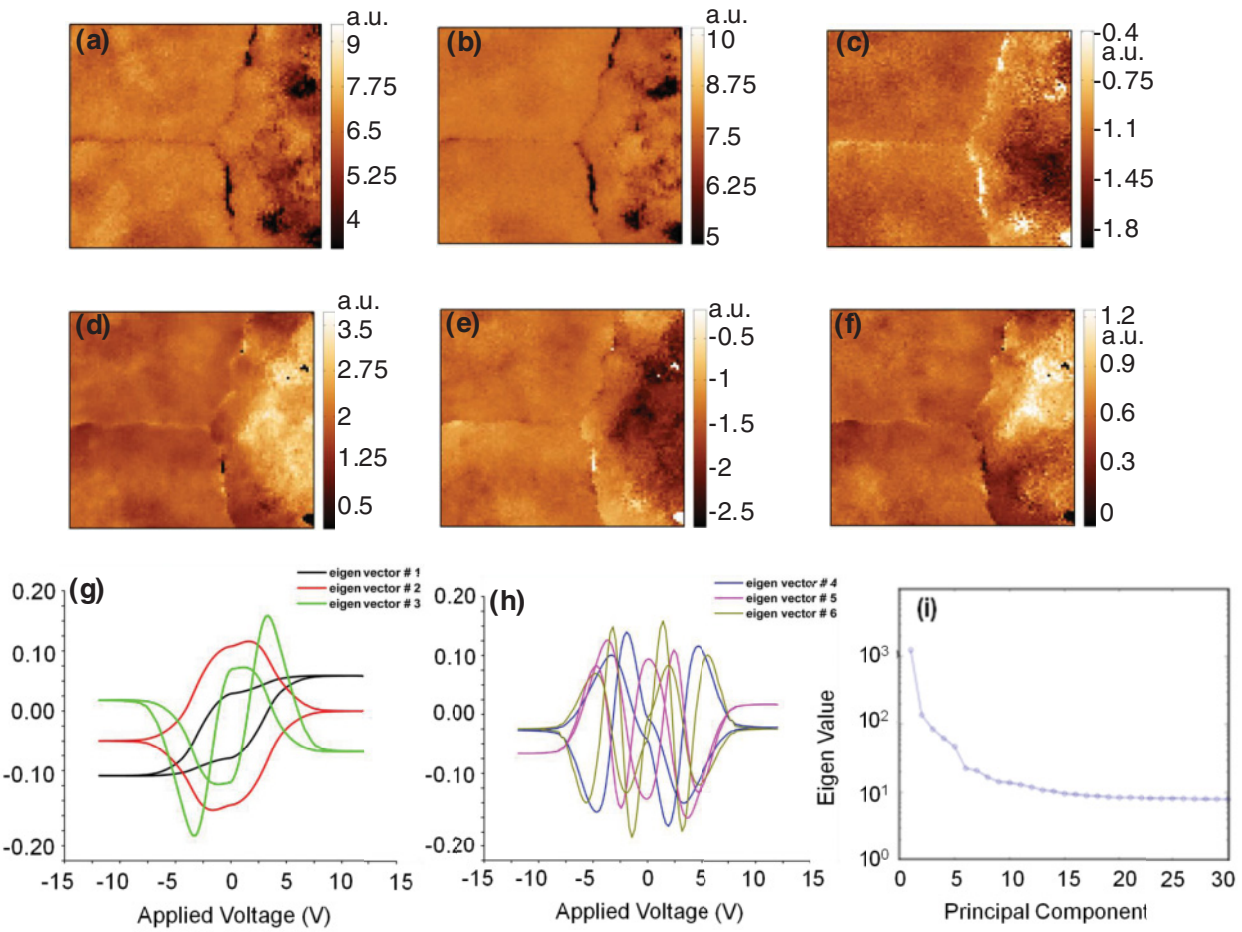

FIG. 8. (Color online) (a)–(f) Loading maps for first six PCA components, (g) normalized eigenvectors for first three PCA components, and (h) normalized eigenvectors for next three PCA components. (i) Plot of eigenvalue versus principal-component number (scree plot) suggesting that PCA components above 10 do not have significant correlation and hence do not provide information about the adopted model.

beyond an optimum leads to overtraining of the network and emergence of spurious minima.[67] The software is implemented using Neural Network Toolbox for MatLab. The trained neural network acts as a universal interpolator that establishes the relationship between the hysteresis loop described as coefficients $a_k(J_0,\delta J,\delta h)$ in the basis of linearly independent eigenvalues $w_k(H_j)$ and model parameters $J_0,\delta J,\delta h$. Note that in this approach the finer details of the hysteresis-loop shape (as described by the higher PCA components) are weighted equally with the gross features in the hysteresis loop, unlike the straightforward least square error-based criterion.

On the analysis stage the same set of $w_k(H_j)$ is used to project unknown experimental loops $S_{\rm exp}(H)$ (after proper normalization) on to a set of $\alpha_{i\_{\rm exp}}$ values. The $\alpha_{i\_{\rm exp}}$ are then fed into the neural net trained by theoretical curves to yield $J_0,\delta J,\delta h$. This effectively forms a solution algorithm to the inverse problem of Eq. (1), i.e., reconstruction of disorder parameters from the hysteresis loop shape.

IV. RESULTS AND DISCUSSION

The local hysteresis loops were processed to extract vertical (offset) and horizontal (imprint bias) shifts and normalized by width (coercive bias) and height (maximal response), thus normalizing the data. The corresponding parameters are illustrated in Fig. 7. The position dependence of these parameters yields *normalization parameter* maps, which are similar to phenomenological descriptors of ferroelectric behavior.

In order to reconstruct the disorder parameters from the hysteresis loops, the experimental loops are projected onto the eigenvectors that are obtained by running PCA on the simulated loops. The loading maps of a_{mk} that represent the map of expansion coefficients in Eq. (2) for the first six eigenvectors are shown in Fig. 8(a–f). The eigenvectors used to generate these maps are shown in Fig. 8(g) and (h). These projection maps illustrate the spatial variability of hysteresis-loops behavior in the basis of Ising loop family. Note that the eigenvectors, and hence projection maps, strongly depend on the choice of the model (unlike the direct PCA analysis of the experimental data, which operates on the statistically significant data set and allows for unique decomposition). Furthermore, the number of the nontrivial maps (i.e., those containing visible correlations) provides information on the goodness of the model. If the number of nontrivial maps is small (i.e., less than 5), the model describes the data well. If the number of nontrivial maps is large (greater than 20), the model does not describe the data.

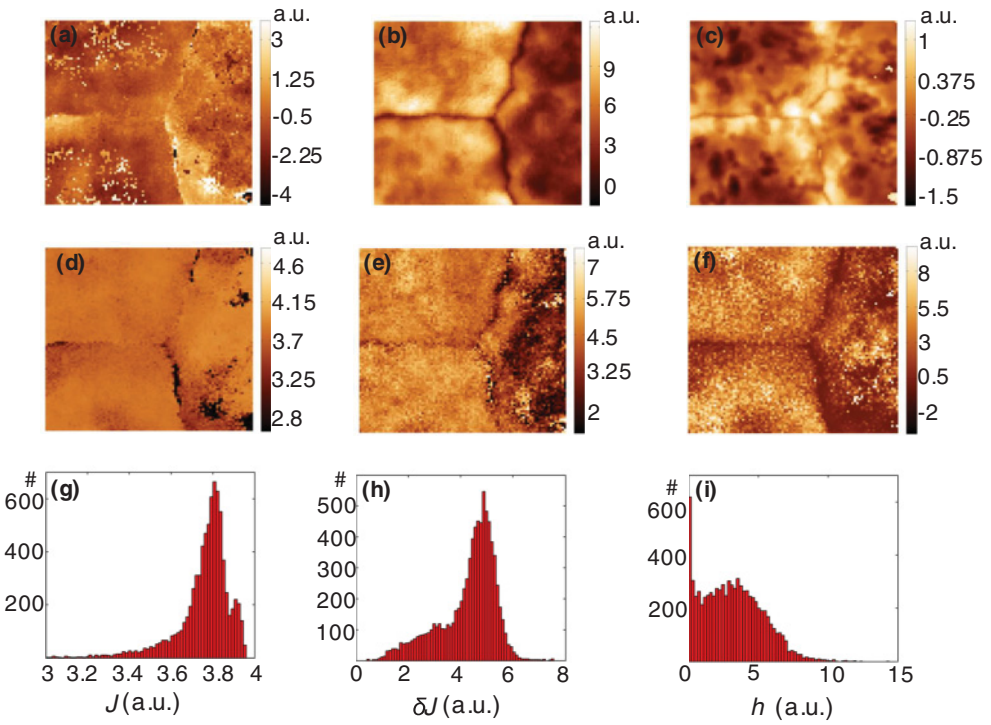

FIG. 9. (Color online) Recognition analysis of the S-PFM data set (90 × 90 spatial pixels, 64 bias points per loop). Top row illustrates normalization parameter maps, including (a) vertical offset, (b) imprint, (c) loop height. The middle row illustrates recognition parameter maps, including (d) J, (e) δJ, and (f) h. Histograms for the reconstructed disorder parameters are (a) J, (b) δJ, and (c) h.

Using the recognition algorithm described in Sec. III A, and III B for a J-δJ-h family (i.e., all three parameters are varied), recognition parameter maps for J, δJ, and h are obtained. A comparison of the normalization parameter maps and recognition parameter maps is shown in Fig. 9(a) – (f). The recognition maps qualitatively capture most of the features observed in the maps obtained from the normalized experimental loops, confirming the validity of the approach used here.

The histograms for the disorder parameters J, δJ, and h shown in Fig. 9(g–i) clearly reveal a distribution of the parameters which most likely arises from the variability in hysteresis behavior across the different grains and cracked regions. Note that the distribution of extracted parameters is relatively narrow, $J_0 = 3.71 \pm 0.35, \delta J = 4.29 \pm 1.07, h = 3.16 \pm 2.18$, with the maximal variability for the built-in field. The correlation functions for the normalization parameters and disorder parameters are shown in Fig. 10(a) and (b), respectively. The correlation function illustrates the presence of spatial correlations

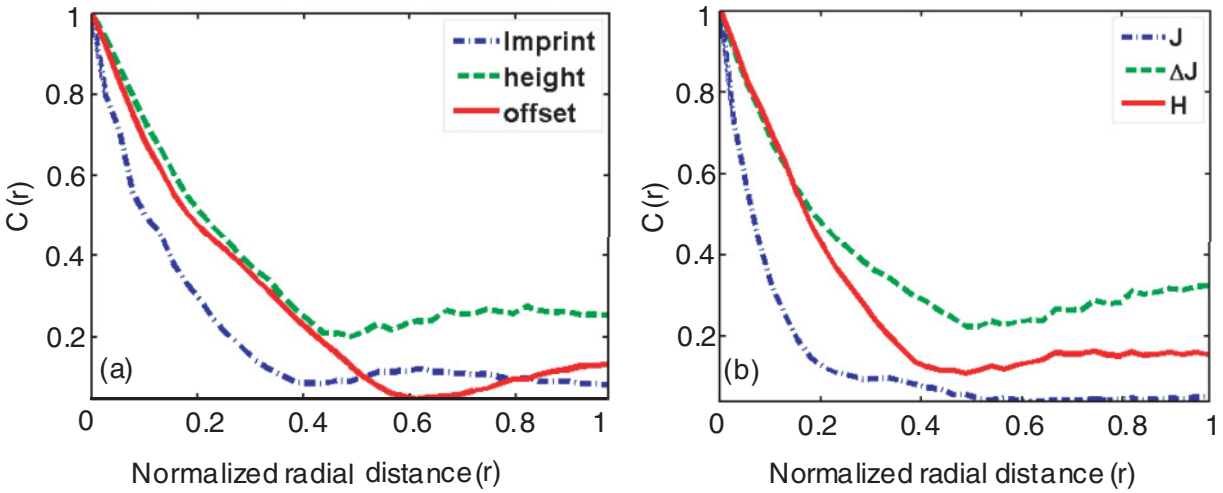

FIG. 10. (Color online) Spatial correlation functions for (a) normalization parameters and (b) reconstructed disorder parameters for the J-δJ-h family. The distance is normalized to image size.

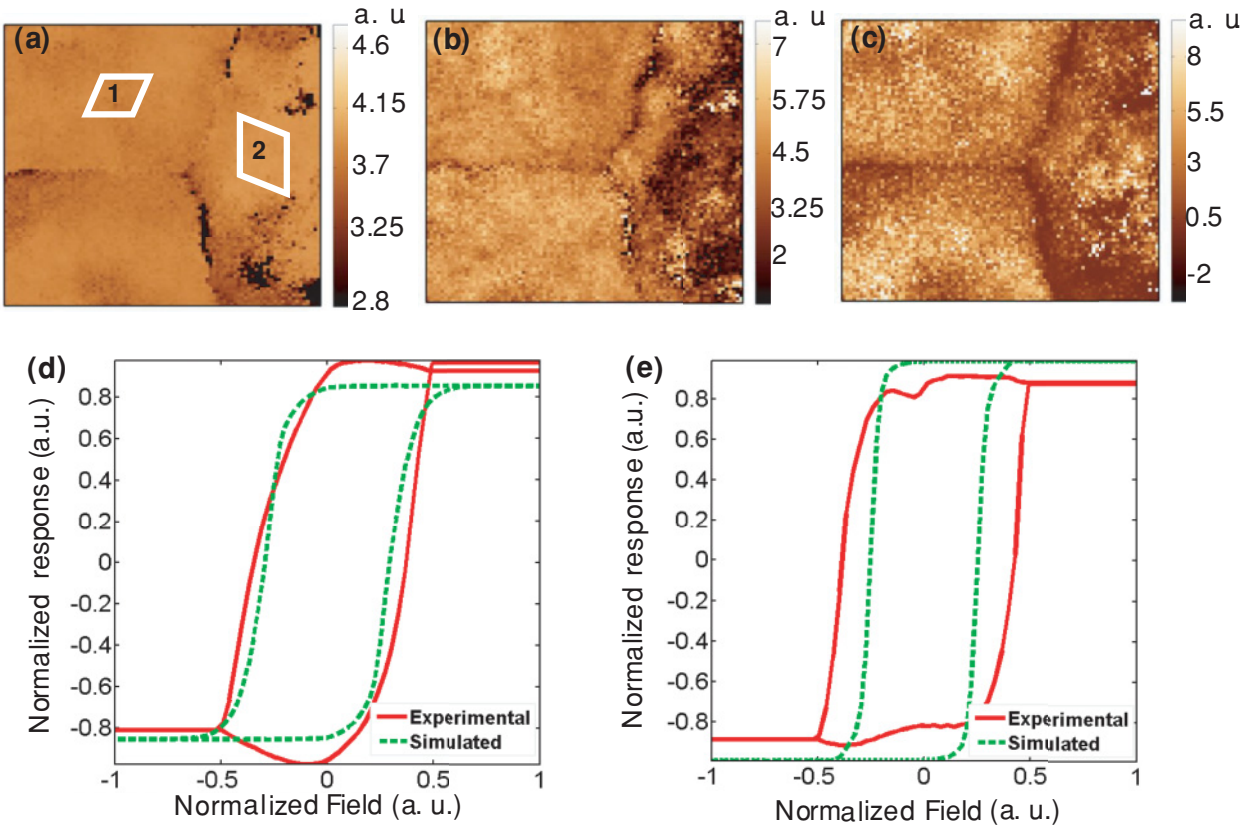

FIG. 11. (Color online) Reconstructed maps for (a) J, (b) δJ, and (c) h for the J-δJ-h family. (d) Average experimental and average of closest simulated loops for the area 1 and (e) area 2 selected in map (a).

in both the normalization parameters as well as the disorder parameters.

The recognition fit for the J-δJ-h family is shown in Fig. 11. For a selected area on the map as shown in Fig 11(a), the average experimental and average of closest simulated loops are shown in Fig. 11(d) and (e). Notice that the "fit" (i.e., the calculated hysteresis loop for the model parameters determined from the neural net recognition) is similar to the target loop. At the same time, both "fit" and "target" have relatively high noise level—from the insufficient averaging in the statistical physics model and experimental noise, respectively. However, the capability to perform such recognition analysis on stochastic data in the absence of analytical expressions is the unique aspect of the recognition fit approach. This allows the underlying physics to be extracted even in the absence of an analytical formulae.

The relatively small variation of model parameters across the sample surface naturally renders a question as to whether a smaller number of parameters would be sufficient to describe the system. Hence, we further explore if the recognition can be performed with a partial parameter set, i.e., J-δJ, J-h, or δJ-h families. Using the recognition fit algorithm, partial families of J-δJ, J-h, or δJ-h are reconstructed as shown in Fig. 12. The performance of average simulated loops extracted from these families in comparison to the normalized experimental loops is shown in Fig. 12(c), (f), and (i) for a selected area. Clearly for the region selected, the J-δJ family outperforms J-h and δJ-h families, thus revealing that choice of different partial families may be better for different grains. This is further exemplified in the fit-quality map obtained by comparing the fitting errors (difference between reconstructed and normalized experimental families) from reconstructed J-δJ, J-h, and J-δJ-h families shown in Fig. 13, which reveals that while the J-δJ family is better than J-h and δJ-h families in two cracked regions, the J-h family is better in the third region. Overall the δJ-h family performs quite poorly in comparison to the other families, which may suggest that these two parameters are not appropriate to describe the system. At the same time the models in which both exchange bias and exchange-bias disorder are allowed to change across the sample surface provide a good description of observed phenomena. The parameters used in the adopted Ising model to describe ferroelectrics are the strength of the grain-grain coupling (analogous to exchange bias) and the disorder in the grain-grain coupling (analogous to exchange-bias disorder). The presence of asymmetries, fine features, and noise in the experimental data precludes more unambiguous model identification.

Based on the analysis above, we conclude that on the length scale of the spectroscopic measurements ($10 > L > 0.3\ \mu$m) the capacitor behaves as an almost spatially uniform random bond-random field (RB-RF) Ising system with strong variability of ferroelectric coupling between the grains ($J_0 \sim \delta J$). The use of spectral imaging reveals the presence of mesoscopic ($\sim 1\ \mu$m) fluctuations in disorder strengths, primarily attributed to the J and δJ terms. Specifically, the switching behaviors are

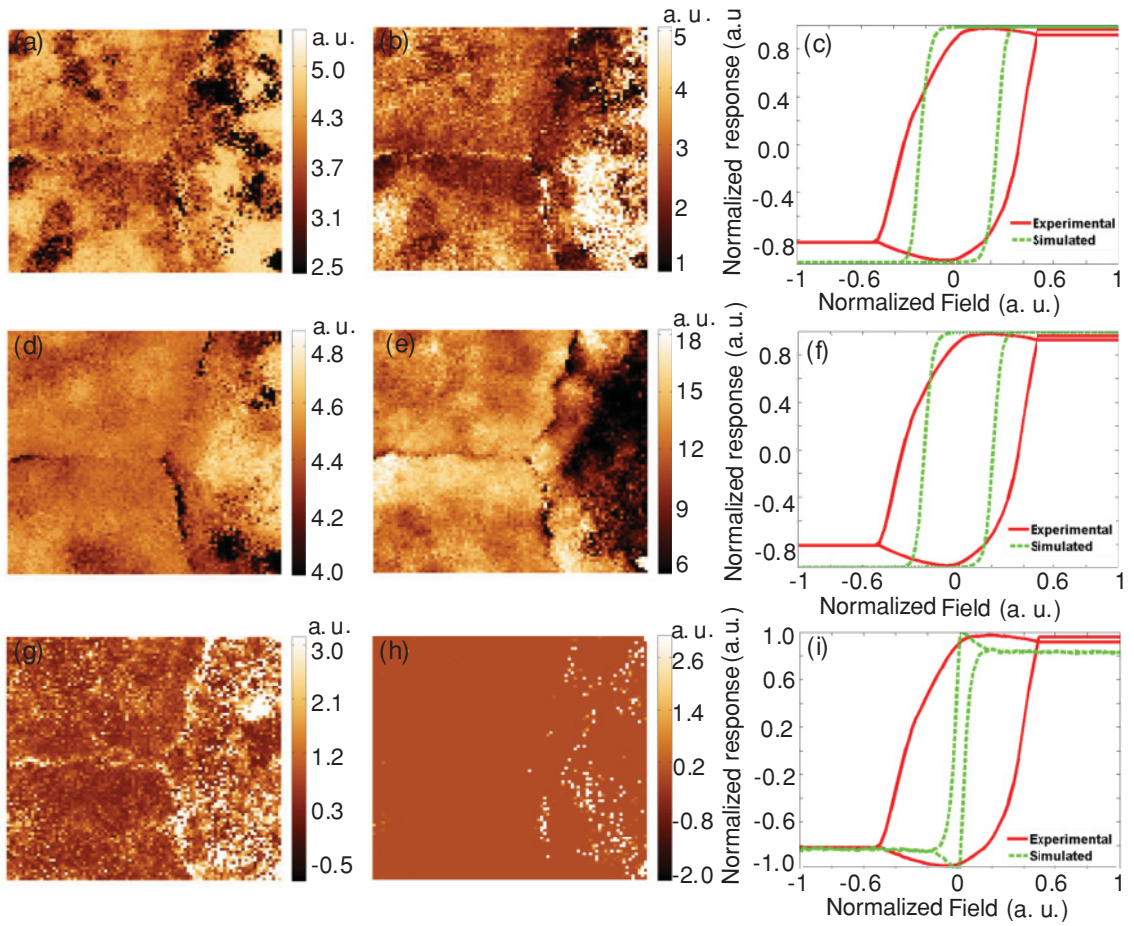

FIG. 12. (Color online) Reconstructed parameters (a) J, (b) δJ, (c) average experimental and closest simulated loops in the selected area for J-δJ family, (d) J, (e) h, (f) average experimental and closest simulated loops in the selected area for J-h family, (g) δJ, (h) h, and (i) average experimental and closest simulated loops in the selected area for δJ-h family.

strongly affected in the vicinity of the crack because of partial strain release and loss of intergrain coupling. Note that the decrease of both J and δJ observed in the reconstructed parameter maps for J-δJ-h families (Fig. 11) close to the crack over a length scale of $\sim$ grain size is in agreement with the chosen Ising-type model with near-neighbor interactions. In comparison larger-scale contrast seen in the field-disorder component is consistent with the strain-induced variations of electromechanical fields on the length scale of the film thickness.

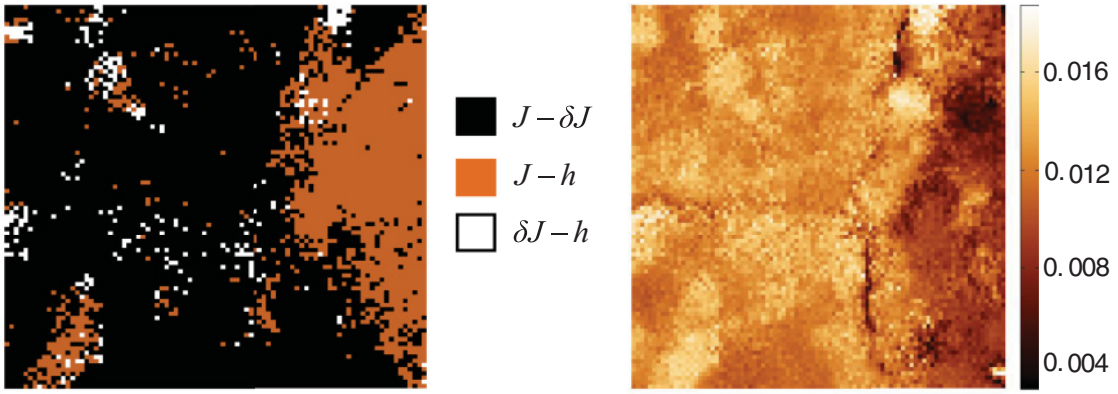

FIG. 13. (Color online) (a) Quality map obtained by comparing the fitting errors (difference between reconstructed and normalized experimental families) from reconstructed J-δJ, J-h, and J-δJ-h families (b) Minimum-error map obtained by comparing the errors from reconstructed families and the best fit between the families is demarcated at each pixel in (a).

V. SUMMARY

Spatially resolved polarization dynamics in polycrystalline-ferroelectric capacitors were studied using BE switching spectroscopy piezoresponse microscopy. The hysteresis loops were analyzed by recognition analysis, mapping the loop shape on the parameters of the random bond-random field Ising model. We demonstrate that the variability of the loop shape is primarily related to the vertical offset and imprint fields and can be interpreted as nonswitchable polarization components, effects of large-scale bending, and the existence of local electrical or mechanical fields. The recognition analysis using several possible parameter sets suggests that both the grain-grain coupling (analogous to exchange interaction) and field-disorder change across the sample surface, and $J \sim \delta J$ (i.e., broad distribution of grain coupling strengths). Given the nonideality of the experimental data, the models (i.e., dominant-disorder type) cannot be further refined.

The recognition analysis of the normalized loops reveals clearly-visible variations in the grain-grain coupling, random bond, and random-field disorder components. The switching behavior is strongly affected in the vicinity of the crack, with both J and δJ decreasing by a factor of $\sim$2, consistent with the loss of intergrain coupling. Finally the random-field component is affected over a larger length scale, presumably as a consequence of the strain fields in the vicinity of the crack. These studies thus provide insight into the spatial variability of disorder strength in the systems with multiple structural length scales and can in the future be linked to the continuum and stochastic models.

In conclusion we note that the hysteretic response is a universal feature of random systems, ranging from strongly correlated oxides to structural (glasses, polymers), magnetic (spin glasses) or polar (dipole glass) to polycrystalline materials. The polycrystalline ferroelectrics capacitors studied here offer a convenient model system, in which the dipole reorientation does not change the underlying crystallographic lattice and hence is (potentially) reversible. At the same time the strong coupling between polarization and strain (lattice deformation) allows the dynamics to be studied locally. The recognition approach developed here is universal and can potentially be applied for arbitrary macroscopic and spatially resolved data, including temperature- and field-dependent hysteresis, I-V curve mapping, electron microscopy electron energy loss spectroscopy (EELS) imaging, and many others.

ACKNOWLEDGMENTS

The research is supported by the ORNL SEED program (S.J. and S.V.K.), Center for Nanophase Materials Sciences (K.S., A.B.P.), ORNL SULI program (O.O.), and in part by CNMS user proposal CNMS2010-090 (F.G. and S.T.M.). Funding for work at Penn State was supplied by a National Security Science and Engineering Faculty Fellowship. The authors gratefully acknowledge Roger Proksch and Asylum Research Corporation for the beta-version of the high-field PFM module.

*Corresponding author: sergei2@ornl.gov

[1] E. Dagotto, *Nanoscale Phase Separation and Colossal Magnetoresistance*, (Springer, Heidelberg, 2003).
[2] K. M. Shen and J. C. S. Davis, Materials Today **11**, 14 (2008).
[3] M. M. Qazilbash, M. Brehm, B. G. Chae, P. C. Ho, G. O. Andreev, B. J. Kim, S. J. Yun, A. V. Balatsky, M. B. Maple, F. Keilmann, H. T. Kim, and D. N. Basov, Science **318**, 1750 (2007).
[4] K. Binder and A. P. Young, Rev. Mod. Phys. **58**, 801 (1986).
[5] A. A. Bokov and Z. G. Ye, J. Mater. Sci. **41**, 31 (2006).
[6] J. P. Sethna, *Statistical Mechanics: Entropy, Order Parameters and Complexity*, (Oxford University Press, Oxford, 2006).
[7] V. Wadhavan, *Introduction to Ferroic Materials*, (CRC, Amsterdam, 2000).
[8] H. G. Katzgraber and G. T. Zimanyi, Phys. Rev. B **74**, 020405 (2006).
[9] J. G. Ramírez, A. Sharoni, Y. Dubi, M. E. Gomez, and I. K. Schuller, Phys. Rev. B **79**, 235110 (2009).
[10] D. Ricinschi, L. Mitoseriu, A. Stancu, P. Postolache, and M. Okuyama, Integrated Ferroelectrics **67**, 103 (2004).
[11] T. Z. Ward, X. G. Zhang, L. F. Yin, X. Q. Zhang, M. Liu, P. C. Snijders, S. Jesse, E. W. Plummer, Z. H. Cheng, E. Dagotto, and J. Shen, Phys. Rev. Lett. **102**, 087201 (2009).
[12] A. Sharoni, J. G. Ramirez, and I. K. Schuller, Phys. Rev. Lett. **101**, 026404 (2008).
[13] G. Catalan, H. Bea, S. Fusil, M. Bibes, P. Paruch, A. Barthelemy, and J. F. Scott, Phys. Rev. Lett. **100**, 027602 (2008).
[14] W. Kleemann, Annu. Rev. Mater. Res. **37**, 415 (2007).
[15] V. V. Shvartsman and A. L. Kholkin, Phys. Rev. B **69**, 014102 (2004).
[16] V. V. Shvartsman and A. L. Kholkin, J. Appl. Phys. **101**, 064108 (2007).
[17] D. Sornette, *Critical Phenomena in Natural Sciences* (Springer, Heidelberg, 2006).
[18] O. S. Ovchinnikov, S. Jesse, P. Bintachitt, S. Trolier-McKinstry, and S. V. Kalinin, Phys. Rev. Lett. **103**, 157203 (2009).
[19] F. Xu, S. Trolier-McKinstry, W. Ren, B. M. Xu, Z. L. Xie, and K. L. Hemker, J. Appl. Phys. **89**, 1336 (2001).
[20] A. Gruverman, B. J. Rodriguez, A. I. Kingon, R. J. Nemanich, A. K. Tagantsev, J. S. Cross, M. Tsukada, and Y. Horii, Appl. Phys. Lett. **83**, 728 (2003).
[21] A. Gruverman, B. J. Rodriguez, A. I. Kingon, R. J. Nemanich, J. S. Cross, and M. Tsukada, Appl. Phys. Lett. **82**, 3071 (2003).
[22] I. Stolichnov, A. Tagantsev, N. Setter, J. S. Cross, and M. Tsukada, Appl. Phys. Lett. **75**, 1790 (1999).
[23] I. Stolichnov, E. Colla, A. Tagantsev, S. S. N. Bharadwaja, S. Hong, N. Setter, J. S. Cross, and M. Tsukada, Appl. Phys. Lett. **80**, 4804 (2002).
[24] D. J. Kim, J. Y. Jo, T. H. Kim, S. M. Yang, B. Chen, Y. S. Kim, and T. W. Noh, Appl. Phys. Lett. **91**, 132903 (2007).
[25] R. Gilles, Ph.D. Thesis, École polytechnique fédérale de Lausanne (EPFL), Lausanne 2001.

[26]F. Griggio and S. Trolier-McKinstry, J. Appl. Phys. **107**, 024105 (2010).
[27]F. K. Lotgering, J. Inorg. Nucl. Chem. **9**, 113 (1959).
[28]W. Cao and C. A. Randall, J. Phys. Chem. Solids **57**, 1499 (1996).
[29]P. Bintachitt, S. Trolier-McKinstry, K. Seal, S. Jesse, and S. V. Kalinin, Appl. Phys. Lett. **94**, 042906 (2009).
[30]A. Gruverman and A. Kholkin, Rep. Prog. Phys. **69**, 2443 (2006).
[31]N. Balke, I. Bdikin, S. V. Kalinin, and A. L. Kholkin, J. Am. Ceram. Soc. **92**, 1629 (2009).
[32]A. Batagiannis, M. Wubbenhorst, and J. Hulliger, Curr. Opin. Solid State Mater. Sci. **14**, 107 (2010).
[33]M. Alexe and A. Gruverman, Eds., *Nanoscale Characterization of Ferroelectric Materials*, (Springer, Heidelberg, 2004).
[34]S. Hong, Ed., *Nanoscale Phenomena in Ferroelectric Thin Films*, (Kluwer, Dordrecht, 2004).
[35]S. V. Kalinin, B. J. Rodriguez, S. H. Kim, S. K. Hong, A. Gruverman, and E. A. Eliseev, Appl. Phys. Lett. **92**, 152906 (2008).
[36]S. Jesse, S. V. Kalinin, R. Proksch, A. P. Baddorf, and B. J. Rodriguez, Nanotechnology **18**, 435503 (2007).
[37]C. Harnagea, M. Alexe, D. Hesse, and A. Pignolet, Appl. Phys. Lett. **83**, 338 (2003).
[38]S. Jesse, B. Mirman, and S. V. Kalinin, Appl. Phys. Lett. **89**, 022906 (2006).
[39]B. Mirman and S. V. Kalinin, Appl. Phys. Lett. **92**, 083102 (2008).
[40]R. Proksch and E. D. Dahlberg, Rev. Sci. Instrum. **64**, 912 (1993).
[41]M. Stark, R. Guckenberger, A. Stemmer, and R. W. Stark, J. Appl. Phys. **98**, 114904 (2005).
[42]B. J. Rodriguez, C. Callahan, S. V. Kalinin, and R. Proksch, Nanotechnology **18**, 475504 (2007).
[43]A. B. Kos and D. C. Hurley, Meas. Sci. Technol. **19**, 015504 (2008)
[44]R. Nath, Y. H. Chu, N. A. Polomoff, R. Ramesh, and B. D. Huey, Appl. Phys. Lett. **93**, 072905 (2008).
[45]R. Proksch and S. V. Kalinin, Nanotechnology **21**, 455705 (2010).
[46]S. Guo, O. Ovchinnikov, M. E. Curtis, M. B. Johnson, S. Jesse, and S. V. Kalinin, J. Appl. Phys. **108**, 084103 (2010).
[47]H. Y. Guo, J. B. Xu, I. H. Wilson, Z. Xie, E. Z. Luo, S. B. Hong, and H. Yan, Appl. Phys. Lett. **81**, 715 (2002).
[48]I. D. Kim, Y. Avrahami, H. L. Tuller, Y. B. Park, M. J. Dicken, and H. A. Atwater, Appl. Phys. Lett. **86**, 192907 (2005).
[49]S. V. Kalinin, A. Gruverman, and D. A. Bonnell, Appl. Phys. Lett. **85**, 795 (2004).
[50]L. M. Eng, H. J. Güntherodt, G. Rosenman, A. Skliar, M. Oron, M. Katz, and D. Eger, J. Appl. Phys. **83**, 5973 (1998).
[51]B. J. Rodriguez, A. Gruverman, A. I. Kingon, R. J. Nemanich, and J. S. Cross, J. Appl. Phys. **95**, 1958 (2004).
[52]R. Desfeux, C. Legrand, A. Da Costa, D. Chateigner, R. Bouregba, and G. Poullain, Surf. Sci. **600**, 219 (2006).
[53]S. Jesse, P. Maksymovych, and S. V. Kalinin, Appl. Phys. Lett. **93**, 112903 (2008).
[54]S. Jesse, H. N. Lee, and S. V. Kalinin, Rev. Sci. Instrum. **77**, 073702 (2006).
[55]A. Agronin, M. Molotskii, Y. Rosenwaks, G. Rosenman, B. J. Rodriguez, A. I. Kingon, and A. Gruverman, J. Appl. Phys. **99**, 104102 (2006).
[56]M. Molotskii, A. Agronin, P. Urenski, M. Shvebelman, G. Rosenman, and Y. Rosenwaks, Phys. Rev. Lett. **90**, 107601 (2003).
[57]M. Molotskii, J. Appl. Phys. **97**, 014109 (2005).
[58]S. V. Kalinin, A. Gruverman, J. Shin, A. P. Baddorf, E. Karapetian, and M. Kachanov, J. Appl. Phys. **97**, 074305 (2005).
[59]S. V. Kalinin, B. J. Rodriguez, S. Jesse, Y. H. Chu, T. Zhao, R. Ramesh, E. A. Eliseev, and A. N. Morozovska, PNAS **104**, 20204 (2007).
[60]S. V. Kalinin, A. N. Morozovska, L. Q. Chen, and B. J. Rodriguez, Rev. Prog. Phys. **73**, 056502 (2010).
[61]Y. P. Shi, L. Hong, and A. K. Soh, J. Appl. Phys. **107**, 124114 (2010).
[62]Z. Chen, S. Haykin, J. J. Eggermont, and S. Becker, *Correlative Learning: A Basis for Brain and Adaptive Systems*, (Wiley, Hoboken, 2007).
[63]S. Haykin, *Neural Networks: A Comprehensive Foundation*, (Macmillan, New York, 1994).
[64]I. T. Jolliffe, *Principal Component Analysis*, (Springer, CITY, 2010.
[65]svd function in Matlab, Mathworks, Inc.
[66]S. Jesse and S. V. Kalinin, Nanotechnology **20**, 085714 (2009).
[67]S. Samarasinghe, *Neural Networks for Applied Sciences and Engineering: From Fundamentals to Complex Pattern Recognition* (Auerbach Publications, Boca Raton, 2006).